Cost-Efficient Prognostics Framework for Heliostat Drive Units

Dominik Steinberg[1,2], Stefan Nicolas Huestegge[(1)], Daniel Maldonado Quinto[3], Marc Röger[4], Benedikt Kölsch[3] and Robert Pitz-Paal[2,3]

[1] *German Aerospace Center (DLR), Institute of Solar Research, Im Langenbroich 13, 52428 Jülich, Germany*
dominik.steinberg@dlr.de
stefan.huestegge@dlr.de (formerly)

[2] *RWTH Aachen University, Chair of Solar Technology, Linder Höhe, 51147 Cologne, Germany*
dominik.steinberg@dlr.de
robert.pitz-paal@dlr.de

[3] *German Aerospace Center (DLR), Institute of Solar Research, Linder Höhe, 51147 Cologne, Germany*
daniel.maldonadoquinto@dlr.de
benedikt.koelsch@dlr.de
robert.pitz-paal@dlr.de

[4] *German Aerospace Center (DLR), Institute of Solar Research, Calle Doctor Carracido 44, 04005 Almería, Spain*
marc.roeger@dlr.de

ABSTRACT

In concentrating solar power tower plants, heliostat drive units are critical components, as they control the precise two-axis alignment of thousands of mirrors, so-called heliostats, that focus incoming solar radiation onto a central receiver. Due to the large field sizes and the corresponding long heliostat–tower distances, even small angular deviations in the milliradian range ($1\,\mathrm{mrad} \approx 0.057°$) result in significant focal point displacements at the receiver. Consequently, the reliable operation of heliostat drive units is essential for the stable and safe operation of solar tower plants.

However, existing research on heliostat operation and maintenance (O&M) predominantly focuses on optical aspects such as mirror soiling (i.e., the accumulation of dust and sand on reflective surfaces), mirror calibration and tracking algorithms, and the influence of wind loads on heliostat performance and structural behaviour. In contrast, the operational health of heliostat drive units remains largely unexplored. To close this research gap, this study presents a cost-efficient prognostics framework for the recording and the subsequent maintenance-oriented analysis of operational data of the heliostat drive units. For this purpose, an extensive measurement campaign is conducted in the heliostat field of the DLR solar tower research facility in Jülich, Germany. In addition to the existing industrial-grade reference sensors and data loggers at the solar tower research facility in Jülich, this study develops a low-cost Arduino-based data acquisition system and performs a comparison between those conventional and cost-efficient monitoring architectures.

The results demonstrate that the recorded measurement data provide a robust foundation for monitoring the heliostat drive units. The proposed prognostics framework is experimentally validated and successfully applied to selected heliostats in the field: first, this shows that sufficiently precise measurements, adequate sampling rates, and straightforward installation and handling can be achieved for field deployment. Second, it demonstrates the capability to identify and analyse real-world operational anomalies. And third, it enables reliable and cost-efficient monitoring significantly reducing the barriers to scalable prognostics and health management (PHM) deployment. Although developed for heliostat drive units, the diagnostics and prognostics methodology presented in this work may be transferable to a wide range of electromechanical systems in industrial PHM applications, as it integrates sensors and instrumentation with anomaly detection, and supports condition-based and predictive maintenance strategies.

1. INTRODUCTION

Within concentrating solar technologies (CST), solar power tower plants are an important technology in which large heliostat fields reflect the incoming solar radiation onto a central receiver mounted on top of a tower. By this, thermal energy is generated that can subsequently be converted into electricity, used for high-temperature industrial process heat, or applied in thermochemical processes.

As shown in Fig. 1, each heliostat typically consists of (i) mirror facets that reflect the incoming sunlight, (ii) a support structure preserving the mirror geometry, (iii) a pylon–foundation system providing structural stability and ground connection, and (iv) drive units that actuate the heliostat to enable continuous two-axis sun tracking by accurately orienting the mirror toward the receiver (Stengler, Bülow, & Pitz-Paal, 2025; Pfahl et al., 2017; Osman & Qureshi, 2025).

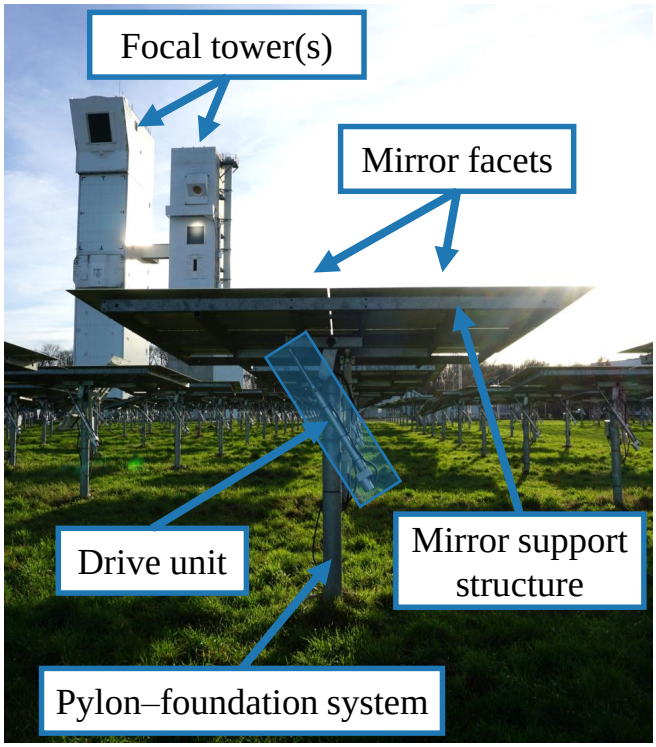

Figure 1. Heliostat field at the DLR solar tower research facility in Jülich, Germany. The central receiver on the top of the focal tower is visible in the background.

The operational reliability of heliostat drive units is therefore crucial for the overall performance of solar tower plants. Failures of these components can lead to considerable maintenance effort and reduced plant availability, while additionally, misdirected solar radiation due to heliostat actuation errors may pose operational and safety risks. It should be noted that due to the large heliostat–receiver distances, even small angular deviations in the heliostat orientation in the milliradian range can lead to significant focal point displacements at the receiver.

Modern heliostat fields usually consist of between 10^3–10^5 heliostats, each equipped with two drive units corresponding to the two rotational axes required for continuous sun tracking. In the context of this work, the terms *heliostat axis* and the corresponding *drive unit* are used synonymously, meaning that the investigation of a given *axis* refers to the drive unit responsible for actuating motion along that axis.

From an operation and maintenance (O&M) perspective, drive units represent a highly critical subsystem for reliable and safe solar tower plant operation. However, maintenance strategies in heliostat fields have traditionally relied on corrective or preventive approaches only. Corrective maintenance reacts to failures after they occur, often causing unexpected downtime, whereas preventive maintenance schedules component replacement at predefined intervals, which frequently leads to unnecessary interventions. In contrast, condition-based and predictive maintenance strategies (which are commonly implemented within the broader framework of prognostics and health management (PHM)) are designed to monitor the actual operational state of components or subsystems and thereby allowing the detection of deviations from normal behaviour at an early stage (Zio, 2022; Calabrese, Regattieri, Bortolini, Gamberi, & Pilati, 2021; Ali & Abdelhadi, 2022).

The large number of heliostats in utility-scale plants represents a key challenge for the development of such advanced monitoring solutions for heliostat drive units, necessitating technically robust, economically scalable, and easily deployable monitoring approaches. This motivates cost-efficient and non-intrusive sensing concepts that can be integrated with minimal installation effort. Low-cost sensors offer several advantages compared to conventional industrial-grade monitoring equipment, including significantly lower hardware costs, smaller size, reduced weight, and lower power consumption. Combined with low-cost microcontroller platforms, these sensing solutions enable scalable monitoring architectures aligned with Industry 4.0 paradigms including IoT connectivity, big data analytics, and predictive maintenance strategies (Cannavacciuolo, Ferraro, Ponsiglione, Primario, & Quinto, 2023; Achouch et al., 2022; Aoun, Ilinca, Ghandour, & Ibrahim, 2021).

Despite these developments in other research and application fields, experimental investigations of such monitoring concepts for heliostat drive units are largely absent, particularly under realistic field operating conditions. Thus, the practical applicability and diagnostic potential of cost-efficient sensing approaches for heliostat condition monitoring have so far received only very limited systematic investigation. To address this gap, the present study develops and experimentally validates a cost-efficient measurement concept for monitoring heliostat drive units and conducts a dedicated field measurement campaign at the DLR solar tower research facility in

Jülich, Germany. In addition, the proposed approach is assessed through a comparison between conventional industrial-grade sensing hardware and a cost-efficient Arduino-based measurement architecture.

2. BACKGROUND AND RELATED WORK

This section reviews the relevant literature from two perspectives: First, research on condition monitoring in the context of heliostat fields (cf. Subsection 2.1); and second, cost-efficient sensing architectures for PHM applications (cf. Subsection 2.2).

2.1. Existing Research on Heliostat Condition Monitoring, Prognostics and Operation and Maintenance

A review of the literature on condition monitoring, prognostics, and O&M of heliostat fields indicates that the mechanical subsystem of the drive units, is generally not considered explicitly in existing studies. Instead, the literature predominantly addresses optical performance, environmental influences affecting heliostat mirrors, and methods aimed at improving heliostat tracking accuracy and calibration.

In particular, many studies examine the effects and the mitigation of *soiling*, which describes the accumulation of dust and sand on reflective surfaces and which can lead to reflectivity degradation and reduced optical efficiency (Sarver, Al-Qaraghuli, & Kazmerski, 2013; Ilse et al., 2019; Wolfertstetter et al., 2020; Wette et al., 2025; Ashley, Carrizosa, & Fernández-Cara, 2019). Another major research direction concerns *wind-induced effects*, focusing on aerodynamic loading and the resulting structural response of heliostats (Emes, Jafari, Pfahl, Coventry, & Arjomandi, 2021; Griffith, Moya, Ho, & Hunter, 2011; Blackmon, 2014; Bakhshipour, Emes, & Arjomandi, 2026; Blume, Röger, & Pitz-Paal, 2023). Furthermore, considerable research efforts have addressed *tracking accuracy* and *calibration*, aiming to minimise optical alignment errors through improved control strategies, calibration procedures (Sattler et al., 2020; Pargmann, Maldonado Quinto, Schwarzbözl, & Pitz-Paal, 2021; Moreno-Cruz, Paredes-Orta, Martell-Chávez, & Salgado-Tránsito, 2025; Schnerring et al., 2026), or image-based measurement approaches (Tian et al., 2026; Schnerring et al., 2025).

In contrast, comparatively little research has addressed diagnostics and prognostics of heliostat drive units. Notably, there are no peer-reviewed studies investigating sensor-based condition monitoring of the heliostat key drive unit components such as the electric motors, gearboxes, or ball-screw mechanisms. Furthermore, to the best of the authors' knowledge, publicly available time-series datasets capturing the operational behaviour of heliostat drive units are currently lacking. This absence significantly constrains the development, benchmarking, and validation of data-driven diagnostics and prognostics approaches for these systems. Consequently, there is a clear research gap regarding sensor-based monitoring methodologies capable of detecting deviations in the operational behaviour of heliostat drive units under real field conditions.

2.2. Existing Research on Cost-Efficient Monitoring Approaches for PHM Applications

In many PHM applications, condition monitoring relies on industrial-grade sensing hardware and data acquisition platforms that offer high accuracy, robustness, and reliability. However, their comparatively high acquisition, installation, and operating costs often limit deployment to only a small number of critical assets, thereby constraining large-scale monitoring in cost-sensitive industrial environments (Jundi, Al-Waeli, & Switzner, 2026; Soto-Ocampo, Mera, Cano-Moreno, & Garcia-Bernardo, 2020; Huang et al., 2024).

To address this limitation, extensive research has explored cost-efficient monitoring options based on low-cost sensors, microcontrollers, and Internet-of-Things (IoT) platforms, including resource-constrained hardware systems e.g. Arduino, or Raspberry Pi (Failing, Abellán-Nebot, Benavent Nácher, Rosado Castellano, & Romero Subirón, 2023; Soto-Ocampo et al., 2020; Mykoniatis, 2020; Villacorta et al., 2021). In particular, numerous studies have demonstrated the feasibility of vibration- and acoustic-based condition monitoring systems implemented on such resource-constrained hardware platforms, often combined with micro-electromechanical- system (MEMS) sensors for signal acquisition (Binali et al., 2024; Kolok, Hodoň, Ševčík, Hotz, & Remy, 2025; Villarroel, Zurita, & Velarde, 2019; Hasibuzzaman et al., 2020; Jakobsen, 2024; Komarizadehasl, Mobaraki, Ma, Lozano-Galant, & Turmo, 2021). These approaches have been successfully applied in several PHM domains, including rotating machinery (Tiboni, Remino, Bussola, & Amici, 2022), manufacturing processes, and industrial equipment monitoring as well as in renewable energy systems such as for photovoltaic power plants (Nkinyam, Ujah, Asadu, Anyaka, & Olubambi, 2025; Hossain, Ali Bashir, & Akter, 2026).

Despite these developments, the application of low-cost sensing architectures to heliostat drive units has, to the best of the authors' knowledge, not yet been investigated in the literature. However, the proven effectiveness of these approaches in other PHM applications provides strong motivation for investigating their applicability to heliostat drive unit monitoring under real field conditions in the present study.

3. METHODOLOGY

To address the research gap identified in Section 2, a dedicated field measurement campaign is conducted using a custom-built, Arduino-based data acquisition platform. The objective of this measurement campaign is to investigate the cost-efficient monitoring of heliostat drive units and to derive diagnostic information from operational sensor signals. For this purpose, vibration and magnetic-field data are acquired directly at the heliostat drive units during operation. The proposed approach follows a prognostics framework. In this context, operational sensor signals are analysed to identify those deviations between the expected baseline behaviour and the actual behaviour that may indicate emerging operational anomalies or maintenance needs.

As illustrated in Fig. 2, the heliostat drive units convert the rotational motion of the electric motor into linear motion via a gearbox and a ball-screw mechanism. Monitoring the dynamic behaviour of these components during operation therefore provides valuable information about the mechanical condition of the drive system.

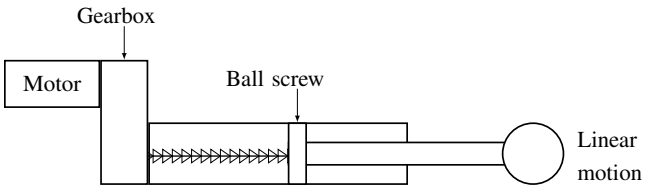

Figure 2. Schematic illustration of a heliostat drive unit as used at the DLR solar tower research facility in Jülich, Germany.

The methodology developed in this study comprises three main elements: (i) the design of a cost-efficient measurement system, (ii) the experimental design for data acquisition during the field measurement campaign, and (iii) the subsequent data analysis and evaluation of the recorded signals.

3.1. Experimental Setup and Measurement Campaign

Regarding the measurable deviations in the operational signals of the heliostat drive units, the experimental design allows to perform comparative analyses both across different heliostats measured under similar conditions and for the same heliostat at different points in time. In particular, the analyses focus on relative deviations from expected baseline behaviour, such as increases in vibration levels or shifts in dominant frequencies in the signal spectrum that may indicate emerging operational anomalies. It should be noted that, in this context, the signals (e.g. vibration signals) are only meaningful while the corresponding heliostat axis is in motion. Therefore, the experiments necessitate controlled movement sequences, which are implemented using dedicated control software developed for the DLR solar tower research facility in Jülich.

The data have been collected during the measurement campaign spanning five months (from July 2025 to November 2025) in the heliostat field of the DLR solar tower research facility in Jülich (cf. Fig. 1) which comprises more than 2,000 heliostats (Göhring, Kaufhold, Quinto, Sibum, & Wirger, 2023). For the present study, a representative subset of eight heliostats has been instrumented, and measurements were performed on both drive units of each heliostat. (The IDs of these heliostats are: 12023, 12024, 12025, 12026, 12123, 12124, 12125, and 12126.) Rather than continuous long-term monitoring, the measurement campaign consisted of a series of controlled short-term experimental runs, each lasting from several hours up to a few days. The experiments were repeated multiple times to ensure reproducibility of the observed signal characteristics. In total, data with 330 hours of effective measurement time (approximately 110 GB of measurement data) have been recorded. Selected measurement results are presented and discussed in Section 4.

3.2. Measurement System

The proposed measurement system is based on an Arduino-based data acquisition architecture which is depicted in Fig. 3. In brief, analogue sensor signals are either routed directly to the Arduino microcontroller or passed through an optional analogue signal conditioning stage before digitisation and subsequent transmission to the measurement computer or, alternatively, to USB storage. For this work, an Arduino GIGA R1 WiFi is used, which is based on the STM32H747XI microcontroller (Arduino datasheet, 2026).

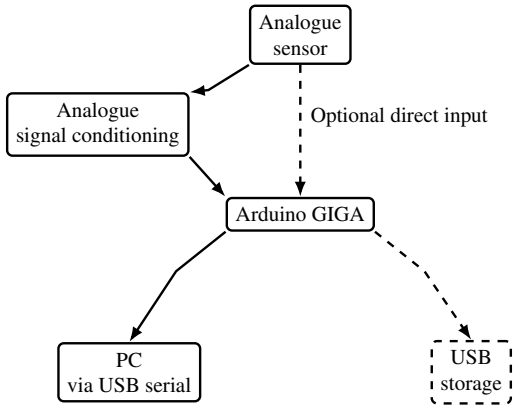

Figure 3. Functional schematic of the Arduino-based measurement system.

Data Acquisition and Logging Architecture The sensor signals are sampled at a rate of $f = 1.0\,\mathrm{kHz}$ while the achievable maximum sampling rate $f_{\max}$ depends on the number and type of connected sensors as well as on the stability of the data transmission. Therefore, extensive preliminary experiments have been conducted to determine stable data logging operating conditions. For a single sensor channel, a maximum

stable sampling rate of approximately $f_{\max} \approx 7.65\,\mathrm{kHz}$ was achieved. Thus, the selected sampling rate of $f = 1.0\,\mathrm{kHz}$ is conservative yet sufficient for the monitoring task, while maintaining a considerable performance margin for future applications.

During the heliostat operation, the sensor data are continuously streamed via USB serial communication to a measurement computer. Each received data packet is assigned a UNIX timestamp and, for efficient handling of larger datasets, the data are stored in HDF5 format, which provides a structured and highly efficient container for such large time-series datasets. Moreover, basic consistency checks are performed and potential transmission errors are handled by the developed custom Python-based logging and storing script.

In a final processing step, the raw digital sensor readings are converted into physical quantities. The analogue-to-digital converter (ADC) values are first converted into voltages, which are then mapped to the corresponding physical units using the sensor-specific calibration parameters (offset and sensitivity). For all sensors, additional calibration measurements were performed to improve measurement accuracy.

Sensor Selection and Rationale For each heliostat axis, two types of analogue sensors are installed: one Hall-effect sensor (providing 1 measurement value) and one MEMS-based 3-axis accelerometer (providing 3 measurement values). Consequently, a total of four sensor channels are recorded per heliostat axis.

Digital sensors are deliberately not employed in the present setup, as they typically impose limitations on the achievable stable sampling rate. This is because most digital sensors communicate with the Arduino via the *Inter-Integrated Circuit* (I^2C) interface which is a serial communication bus using two lines: SCL (serial clock) and SDA (serial data). Preliminary experiments performed during this study confirmed that I^2C-connected sensors require significantly more communication time than directly sampled analogue sensors. Nevertheless, the Arduino-based architecture would in principle also allow the integration of digital sensors if required for other applications.

Analogue Signal Conditioning To utilise the input range of the Arduino ADC as efficiently as possible, an analogue signal-conditioning stage is implemented based on preliminary experiments. The circuit comprises a first-order RC high-pass filter, a voltage divider introducing a DC offset, and a non-inverting amplifier. The high-pass filter suppresses low-frequency components, while the offset shifts the signal into the usable ADC input range. The non-inverting amplifier increases the signal amplitude and thereby improves the effective resolution of the subsequent digitisation.

The circuit parameters are determined based on the experimental requirements and are validated through preliminary measurements. Although a theoretical maximum gain of approximately $V \approx 33$ is possible, a nominal gain of $V = 11.5$ was selected to avoid saturation in the presence of abnormal vibration amplitudes. The experimentally measured gain is $V = 11.6$, which is consistent with the expected tolerances of the analogue components and the Arduino ADC. Experimental verification has confirmed that the signal-conditioning stage both exhibits a linear response within the relevant measurement range and does not introduce significant additional measurement errors. Moreover, the amplification improves the signal-to-noise characteristics of the recorded measurements.

ADC Resolution and Measurement Uncertainty The ADCs of the STM32H747XI microcontroller used in this study are configured with a resolution of 16 bit (STM32H747 datasheet, 2026). For the analogue input range considered here, defined by $U_{\mathrm{ref}-} = 0.0\,\mathrm{V}$ and $U_{\mathrm{ref}+} = 3.3\,\mathrm{V}$, the ideal ADC voltage step size ΔU is given by $\Delta U = (U_{\mathrm{ref}+} - U_{\mathrm{ref}-})/2^{16}$, resulting in $\Delta U \approx 50.4\,\mu\mathrm{V}$. This value represents the nominal quantisation resolution and should not be interpreted as the absolute measurement accuracy. The microcontroller datasheet specifies a tolerance of 10 LSB for 16-bit ADC operation, corresponding to an ADC-level tolerance of approximately $10 \cdot 50.4\,\mu\mathrm{V} \approx 0.50\,\mathrm{mV}$.

The overall measurement uncertainty is affected by several factors, including reference-voltage stability, ADC offset and gain errors, sensor accuracy, temperature drift, and electromagnetic interferences. To improve measurement precision, the measurement value of each analogue sensor was obtained by averaging $m = 8$ consecutive ADC readings. For predominantly uncorrelated random noise, this reduces the standard deviation of the random noise component by $1/\sqrt{m} = 1/\sqrt{8} \approx 0.354$. Preliminary experiments confirmed that this procedure stabilises the analogue readings, while the additional repeated ADC reading operations did not constitute a computational bottleneck for the chosen configuration. While this averaging reduces random fluctuations, it does not compensate for systematic uncertainty contributions such as calibration errors, reference-voltage deviations, ADC non-linearities, or a potential sensor bias.

Overall, the uncertainty of the measurement chain is considered acceptable in the context of this work, given that the proposed monitoring approach is focused on identifying deviations between the expected baseline behaviour and the actual operational behaviour as indicators of emerging anomalies or maintenance requirements, rather than on highly accurate absolute measurement values.

Sensor Mounting and Field Instrumentation For the sensor installation, first the motor housing cover has to be removed. Afterwards, a custom designed metal sensor mounting

plate with pre-drilled threaded holes is screwed into the underside of the motor. This plate enables various sensors, including industrial-grade vibration sensors, to be indirectly mounted to the motor while ensuring a rigid, near 1:1 mechanical coupling.

The 3-axis accelerometer is mounted on this plate as shown in Fig. 4a. Due to the geometrically predefined mounting position, sensor orientation only affects the sign of the measured acceleration in the x- and y-directions. In contrast, the Hall-effect sensor is mounted laterally on the motor housing as depicted in Fig. 4b. Since the motor wall is thin and the internal coils are located directly beneath it, screw fixation is not feasible. Instead, waterproof outdoor adhesive tape is tightly wrapped around the motor, and the sensor is fixed onto this layer with additional tape. Correct sensor orientation must be ensured, as the employed Hall sensor captures the magnetic field along one single measurement-axis.

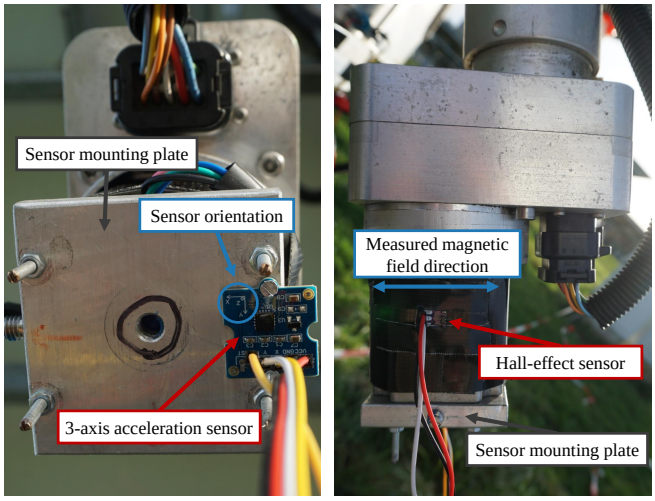

(a) 3-axis accelerometer mounted on the metal sensor mounting plate.

(b) Hall-effect sensor mounted laterally on the motor housing.

Figure 4. Installation of the Arduino-based sensors on the motor of one heliostat axis.
Color coding: red = sensors; blue = measurement directions/ orientation information; dark gray = additional annotations.

The installation procedure has to be carried out separately for both heliostat axes. Once mounted, the sensors are connected to the analogue signal conditioning unit which is then connected to the Arduino (cf. Fig. 3). The wiring scheme is as follows: the sensors are powered via the Arduino 5 V supply pin and connected to ground through the GND pin. The analogue sensor signals, either directly from the sensor or after signal conditioning, are routed to the Arduino analogue input pins. As a wiring simplification approach, a Grove shield is mounted on the Arduino, enabling straightforward connection via Grove (Grove system by Seeed Studio) extension cables. During the measurements, large heliostat movements are actively induced; therefore, the cables must provide sufficient slack to compensate for the resulting change in distance between sensors and the Arduino. Depending on the experimental setup, cable slack of up to 50% may be required. For outdoor operation, the sensors are coated with an electronics protective lacquer to prevent moisture ingress, while keeping the electrical connectors uncovered. The Arduino microcontroller itself is placed in a weatherproof enclosure at the base of the heliostat.

4. EXPERIMENTAL RESULTS AND DISCUSSION

The analysis presented in this section focuses on illustrative data comparisons and frequency-domain methods such as the FFT and the short-time Fourier transform (STFT). The latter provides a time-resolved representation of the signal spectrum and thereby allows changes in dominant frequencies to be observed over the course of a measurement.

4.1. Validation of the Prognostics Framework: Analogue Signal Conditioning Proof-of-Concept and Sensor Comparison

Using the extensive set of measurements collected during the field campaign, the Arduino-based data acquisition system introduced in Section 3 has been validated. This section presents representative results illustrating the quality and characteristics of the recorded operational data obtained using analogue signal conditioning. In addition, a quantitative comparison between conventional industrial-grade sensors and the proposed cost-efficient sensor architecture is performed. It should be noted that the measurement system was developed through an iterative process involving multiple preliminary tests and successive experimental refinements during the field measurement campaign.

Characteristics of the Recorded Operational Data Using Analogue Signal Conditioning In Fig. 5 and Fig. 6, the signals for Axis 1 recorded by the 3-axis acceleration sensor are shown. The sensor measures vibrations in three directions: two transversal directions (North–South and East–West) and one axial direction, which is, by definition, aligned with the actuator motion (extension/retraction). The North–South designation refers to the real-world geographical coordinate system. During the measurement, the two heliostat axes were actuated in a sequence of nine movement steps (labelled from a) to i)), including individual, simultaneous, and opposing extension and retraction movements, as documented in Table 1.

Comparing Fig. 5 (raw signal without analogue signal conditioning) and Fig. 6 (with analogue signal conditioning), the effect of the analogue signal conditioning becomes clearly visible: the reason for the pronounced sawtooth-like behaviour of the blue curve in Fig. 5 is that the 3-axis accelerometer intrinsically measures the gravitational accelera-

tion g in addition to the dynamic vibration components. During heliostat motion, the mirror structure changes its orientation in space, which causes the projection of the gravitational acceleration onto the three sensor axes to vary over time. As a result, the measured acceleration signal is dominated by the slowly varying gravity component, which masks the actual vibration signatures.

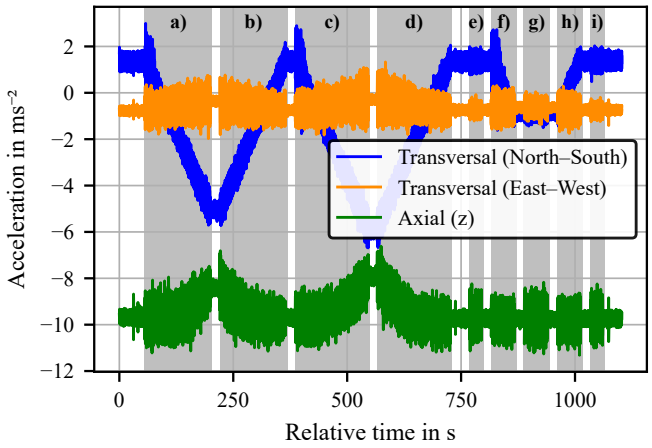

Figure 5. Raw 3-axis accelerometer signals measured at Axis 1 during the nine-step movement sequence defined in Table 1. The shaded grey regions indicate the individual movement intervals. It should be noted that the signals include the gravitational acceleration g, which leads to comparatively large acceleration amplitudes.

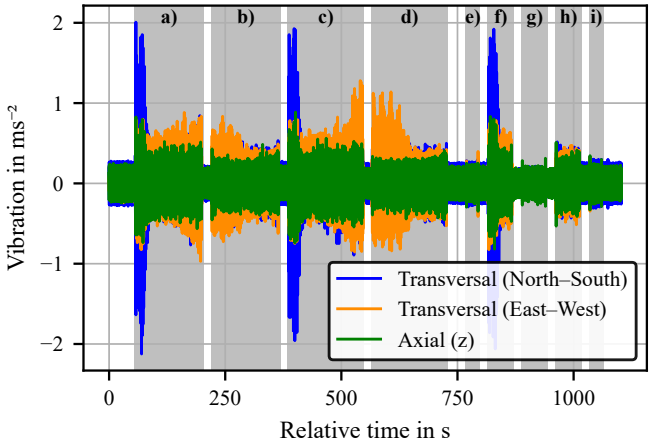

Figure 6. 3-axis vibration signals measured at Axis 1 during the nine-step movement sequence defined in Table 1 including the analogue signal conditioning. The gravitational acceleration component g is removed by the conditioning stage; therefore, the y-axis shows the resulting *vibration* signal.

The results shown in Fig. 6 confirm that this effect is effectively removed by the analogue signal conditioning stage. Moreover, the signal is centred around the zero line, thereby yielding measurement signals that are more interpretable. For all subsequent analyses, the conditioned signal is therefore used. During the nine movement steps visualised in Fig. 6, the vibration level is noticeably increased compared with the time intervals in which the heliostat remains stationary, where only background noise is recorded.

Furthermore, distinct differences in the vibration patterns can be observed between the movement steps a)–i). As an illustrative example, the intervals e), g), and i) show only minor vibration increases above the background noise level. According to Table 1, only Axis 2 is actuated during these steps, while Axis 1 remains stationary. The observed signals therefore originate solely from mechanical coupling effects between the two axes. Although the vibration patterns observed in the remaining movement steps are likewise physically explainable, their detailed interpretation is beyond the scope of this validation section. Overall, the results indicate that the developed analogue signal conditioning represents a practical and effective approach for improving the quality and interpretability of the recorded sensor signals.

Table 1. Overview of the heliostat axes movements during the measurements presented in Fig. 5 and Fig. 6. Legend: ↑ axis is extended; ↓ axis is retracted; − axis is not moved. It should be noted that the movement steps differ in their step lengths: steps a)–d) correspond to longer movements, whereas steps e)–i) represent shorter movement cycles with fewer actuator steps.

Movement	a)	b)	c)	d)	e)	f)	g)	h)	i)
Axis 1	↑	↓	↑	↓	−	↑	−	↓	−
Axis 2	↓	↑	↑	↓	↓	−	↑	−	↓

Comparison of Conventional Industrial-Grade Sensors and Cost-Efficient Arduino-Based Sensors A qualitative comparison between the industrial-grade reference sensors and the Arduino-based measurement system is presented in Fig. 7, which shows approximately 1.5 s of data during the start-up phase of the heliostat motor. Around $t \approx 0.25$ s the motor start-up begins, characterised by decreasing current amplitudes and increasing signal frequency over time. The two current clamp signals (blue and orange curves) measure the currents in the two motor phases, while the Hall-effect sensor (green curve) records the resulting magnetic field generated by these currents.

This qualitative comparison shows a strong correspondence between the measured current signals and the magnetic field signal, including a characteristic double-peak structure in the magnetic field that aligns with the peaks of the two phase currents. This indicates that the low-cost Hall-effect sensor is capable of capturing a signal that is very closely related to the motor current behaviour, demonstrating that the Arduino-based system provides a viable alternative for monitoring purposes.

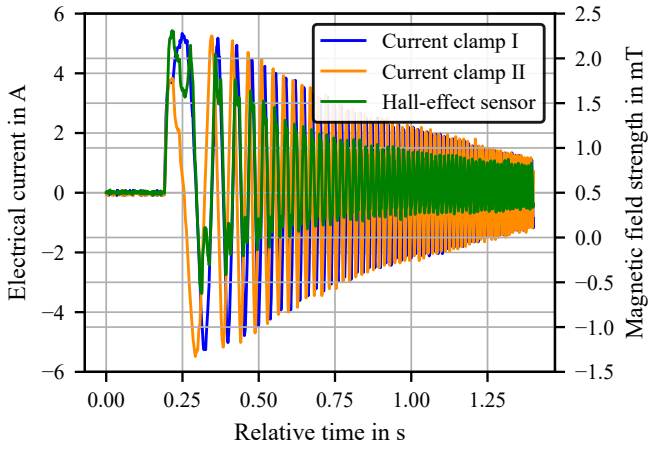

Figure 7. Comparison of motor phase currents measured with two current clamps and the magnetic field measured with a Hall-effect sensor during the start-up phase of the heliostat motor. Current Clamp I and Current Clamp II are attached to the two motor phase conductors, while the Hall-effect sensor measures the resulting magnetic field generated by both phase currents.

However, a limitation of the Hall-effect sensor becomes apparent when magnetic fields from both heliostat axes overlap. During one test measurement, the heliostat orientation temporarily brought the motors of both axes into close proximity, causing a superposition of their magnetic fields. While such effects can be identified and corrected during the subsequent data analysis, current clamps are inherently less susceptible to this interference because they measure the current directly at the conductor. Nevertheless, the Hall-effect sensor offers a significant practical advantage since it can be installed externally without requiring direct access to the current-carrying wires, which greatly simplifies sensor installation in outdoor field conditions.

4.2. Sensitivity Analysis of the Prognostics Framework: Controlled Variations of the Motor Phase Resistance

In order to assess the sensitivity of the prognostics framework introduced in Section 3, a controlled experiment was conducted in which characteristic signal signatures were deliberately induced in the measurement data. The analysis presented here serves as an exemplary system-level validation. In this context, the primary focus is placed on the magnetic field strength, although the vibration measurements are also considered in the discussion.

Concept of the Experimental Study with Controlled Motor Phase Resistance Variation The underlying idea of this experiment is to intentionally modify the electrical operating conditions of the motor in order to induce measurable changes in the magnetic field, which may also lead to observable variations in the vibration behaviour. In order to experimentally realise this modification, a measurement campaign is conducted on a randomly selected heliostat in which the electrical operating conditions of the motor is deliberately altered. The motor drive consists of two coil pairs connected to a controller unit. During the experiment, an external resistor R is inserted in series with one of the coil pairs, while the second coil pair remains directly connected to the controller. By varying the value of R, the electrical load of the affected phase is systematically adjusted, which alters the current distribution within the motor windings. As a consequence, changes in the resulting magnetic field inside the motor are expected, which can be detected by the Hall-effect sensors.

The resistance R is varied systematically between $R = 0.1\,\Omega$ and $R = 6.1\,\Omega$ using a combined stepping strategy. Around selected operating points, closely spaced resistance pairs with increments of $0.1\,\Omega$ were examined to resolve small changes in the system response, while the overall range is extended in approximately $1\,\Omega$ intervals to cover a broader parameter space. The resistance configuration sequence

$$R \in \{\, 0.0,\ 0.0,\ 0.1,\ 0.2,\ 0.3,\ 0.3,\ 0.5,\ 1.0,\ 1.1,\ 1.2,\ 1.3,\ 1.5,\ 2.0,\ 2.1,\ 3.0,\ 3.1,\ 4.0,\ 4.1,\ 5.0,\ 5.1,\ 6.0,\ 6.1,\ 0.0 \,\}\,\Omega \tag{1}$$

is applied and, in addition, reference measurements without any additional series resistance (i.e. $R = 0\,\Omega$, $0\,\Omega$) were conducted before and after the experiment to provide a baseline for scientific control and to verify measurement stability. The experimental sequence consisted of a systematic variation of the inserted series resistance. For each resistance value R, the same heliostat movement pattern is executed, consisting of an extension and subsequent retraction of the actuator of Axis 1 by 20 000 motor steps. It should be noted that all experiments were performed on Axis 1 only, since Axis 2 is excluded from this analysis. Both axes are electrically identical, so analysing a single axis is considered sufficient.

Magnetic Field Strength Analysis The resulting measurement data obtained from the Hall-effect sensors for Axis 1 are presented in Fig. 8. The experiment spans approximately $t \approx 5{,}000\,\mathrm{s}$ ($\approx 1.4\,\mathrm{h}$). The signal consists of a sequence of characteristic patterns corresponding to the repeated actuator movements of 20 000 steps each. Every pattern exhibits distinct peaks of up to about $1.5\,\mathrm{mT}$ during the motor start-up and braking phases and in between, there is a quasi-stationary phase with a magnetic field amplitude of approximately $0.5\,\mathrm{mT}$ during steady motor operation.

Fig. 8 highlights the global time evolution across the different resistance configurations defined in Eq. (1). These configurations are indicated by dashed vertical grey lines that mark the corresponding resistance intervals (e.g. 0–1 Ω, 1–2 Ω). Since the resistance sequence in Eq. (1) increases monotonically

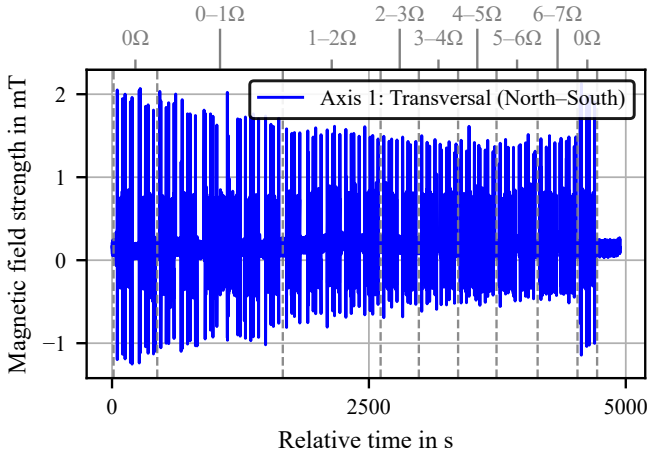

Figure 8. Measured magnetic field strength signal of Axis 1 obtained using analogue signal conditioning. The vertical grey dashed lines indicate the resistance intervals corresponding to the sequence defined in Eq. (1).

(except for the final reference measurement), a reduction in the current through the affected phase is expected from basic circuit considerations (Ohm's law: $U = R \cdot I$). This leads to the observed overall trend (apart from minor fluctuations) of a reduction of the magnetic field amplitude from left to right in the plot in Fig. 8, which is consistent with the physical expectation. For instance, for $R \gtrsim 3\,\Omega$, the magnetic field amplitude is reduced by roughly one third compared with the initial state. At the end of the experiment, the reference measurement with $R = 0\,\Omega$ confirms that the heliostat drive unit returns to its initial operating state, with the magnetic field amplitude recovering to its original level.

Fig. 8 demonstrates that even small changes in the electrical properties of the drive system (here represented by variations in the motor phase resistance) lead to clearly detectable changes in the measured magnetic field signatures. A supplementary trend-based amplitude analysis further suggests that individual $R = 0.1\,\Omega$ increments cannot be resolved reliably, whereas changes on the order of $R = 1\,\Omega$ can be identified with high confidence. In a maintenance context, this sensitivity is highly valuable, as threshold-based comparisons of the signal characteristics enable the early detection of abnormal electrical operating conditions. The affected heliostat can then be directly flagged and prioritised for inspection by the O&M team.

Vibration Analysis During the experimental study presented in this Subsection 4.2, it is observed that, for series resistances above approximately $R \gtrsim 3\,\Omega$, the actuator of Axis 1 exhibits a noticeably increased acoustic emission. This observation motivates an additional inspection of the vibration signals.

As shown in Fig. 9, the FFT spectrum of the vibration signal measured at Axis 1 in the transversal north–south direction reveals clear changes in the frequency domain with increasing additional resistance R. For clarity, only three representative resistance configurations are shown (cf. Eq. (1) and Fig. 8).

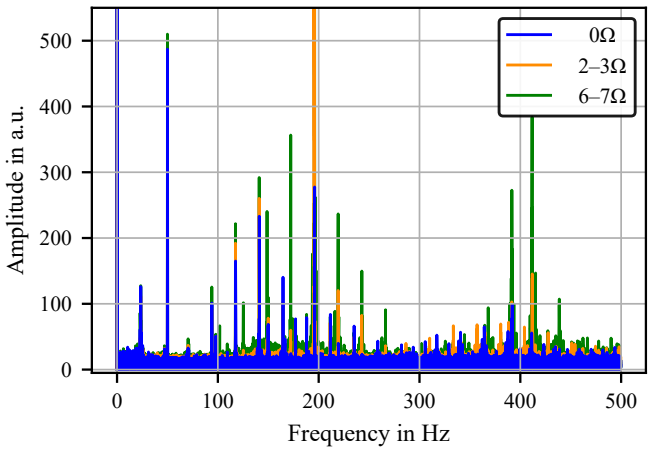

Figure 9. FFT spectra of the measured vibration signals of Axis 1 obtained using analogue signal conditioning. The plotted data refer to the vibration in transversal (North-South) direction. The three curves correspond to representative regions of the resistance configuration sequence defined in Eq. (1).

In particular, for the interval 6–7 Ω (green curve), several vibration peaks are significantly increased compared with the baseline condition $R = 0\,\Omega$ (blue curve). In parts of the higher-frequency range around 400 Hz, amplitude increases of approximately a factor of 2–4 can be observed. These results indicate that the proposed measurement setup is not only very sensitive to variations in the magnetic field strength but also sensitive to vibration changes induced by altered electrical operating conditions of the motor.

Fig. 8 indicates that the R-induced decrease in the magnetic field strength B is consistent with Ohm's law since $R \uparrow \Rightarrow I \downarrow \Rightarrow B \downarrow$. Moreover, Fig. 9 shows that changes in R also affect the vibration spectra which is an effect that cannot be explained by the quasi-static reduction of the current I alone, but requires an interpretation based on time-varying electromagnetic excitation. Preliminary measurements using current clamps showed that the additional resistance R impacted both the current amplitude I and the phase relationship $\Delta\varphi$ between the motor currents. This behaviour is physically plausible given an inductive motor phase, with the current response depending on the complex phase impedance $Z = R + j\omega L$, the current amplitude $|I| = |V|/\sqrt{R^2 + (\omega L)^2}$ and the phase angle $\varphi = \arctan(\omega L/R)$.

The observation that a change in R affects the relative phase position of the motor currents, $\Delta\varphi$, is particularly relevant because smooth motor operation - with low vibration excitation - requires the phase currents to maintain their intended, temporally stable phase offset. For an ideal two-phase motor

with equal current amplitudes and orthogonal phase currents, i.e. $\Delta\varphi = \pi/2$, the current-vector trajectory is circular, corresponding to a nearly uniform rotation of the electromagnetic field and thus, a smooth torque generation. If the additional resistance changes this phase relationship, i.e. $\Delta\varphi \neq \pi/2$, the trajectory becomes elliptical in the Lissajous representation, indicating a non-uniform field rotation. This non-uniform field rotation causes periodic variations in the electromagnetic torque, i.e. torque ripple, which may excite the motor, gearbox, and drive-unit structure at characteristic frequencies as seen in Fig. 9. Therefore, the R-dependent increased vibration peaks can be interpreted as a possible consequence of phase current distortion and the resulting torque ripple.

Although the resistance range around 6–7 Ω as shown in Fig. 9 represents an intentionally exaggerated loading condition that is unlikely to occur during normal operation, similar—albeit weaker—amplitude increases are already observable in the intermediate range around 2–3 Ω (orange curve). This suggests that even moderate electrical deviations can produce detectable changes in the vibration signals.

4.3. Demonstration of the Prognostics Framework: Early Ageing and Anomaly Detection

To demonstrate the cost-efficient prognostics framework proposed in this study, this subsection focuses on the analysis of the measurement data of the drive units of the heliostat with ID 12023. Prior to the measurement campaign, all eight monitored heliostats have been operating under regular plant conditions, and no abnormalities have been reported by the operating personnel. Accordingly, across the monitored heliostats, it is expected to observe a consistent behaviour with typical, characteristic signal patterns. However, in contrast to the other monitored heliostats, the measurement data of the 12023-heliostat exhibit clear deviations from these characteristic signal patterns, indicating anomalous ageing-related behaviour. For this reason, the 12023-heliostat was selected for the detailed analysis presented in this subsection.

Vibration Analysis Fig. 10 and Fig. 11 present the measured vibration signals in transversal (North-South) direction for Axis 1 and Axis 2, respectively (The North-South designation is the same as used in Subsection 4.1.). In addition, Fig. 12 shows the corresponding time-resolved short-time Fourier transform (STFT) of the transversal (North-South) vibration signal for Axis 2. All data were recorded during a single measurement with a total duration $T \approx 13{,}000\,\mathrm{s}$ ($\approx 3.6\,\mathrm{h}$). During this period, the heliostat operated in a cyclic movement pattern, with both axes moving simultaneously and repeatedly extending and retracting throughout the entire measurement.

As can be clearly observed in Fig. 10, the vibration signal initially stabilises at a nearly constant amplitude of approximately $0.4\,\mathrm{m\,s^{-2}}$ during the measurement. However, from about $t \approx 7{,}500\,\mathrm{s}$ onwards, the signal exhibits increasingly pronounced outliers compared with the initial phase. These anomalous peaks reach amplitudes exceeding $1\,\mathrm{m\,s^{-2}}$ and are therefore markedly more pronounced than the previously observed signal fluctuations. Under nominal operating conditions, the vibration level would be expected to remain approximately constant, as observed during the initial phase of the measurement. This expected behaviour was consistently observed across the other seven monitored heliostats.

Comparing the data measured at Axis 1 (cf. Fig. 10) with the data measured at Axis 2 (cf. Fig. 11) reveals similar temporal patterns for the two axes: in both signals, pronounced outlier peaks emerge from approximately $t \approx 7{,}500\,\mathrm{s}$ onwards. For Axis 2, however, these anomalous peaks are considerably more pronounced, reaching amplitudes of nearly $6\,\mathrm{m\,s^{-2}}$, corresponding to approximately ten times the nominal vibration level observed during the initial phase of the measurement. Axis 2 is therefore considered the primary source of the observed vibration anomaly. The weaker vibration response detected on Axis 1 (cf. Fig. 10) is likely attributable to mechanical coupling between the two axes, indicating that the underlying operational issue originates from the Axis 2 drive unit.

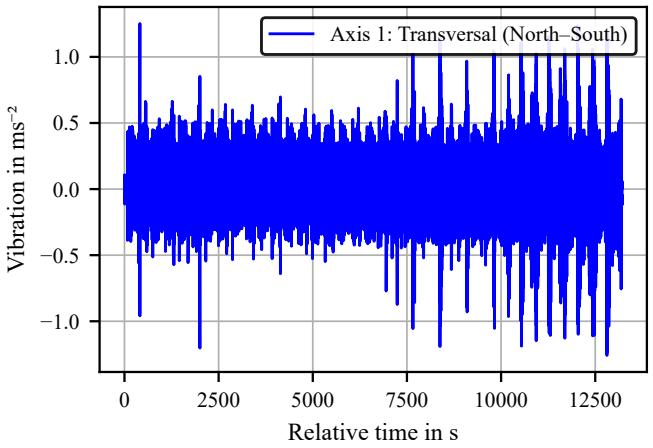

Figure 10. Measured vibration signal of Axis 1 obtained using analogue signal conditioning during the measurement period.

It should be noted that the true peak amplitudes for Axis 2 are likely higher than those shown in Fig. 11, since the sensor signal reaches the upper measurement limit of the data acquisition system (ADC input range: 0 V to 3.3 V cf. Subsection 3.2). Consequently, the peaks visible in Fig. 11 appear clipped at the upper bound of the measurement range. This saturation does not indicate a malfunction of the measurement system. Rather, it confirms that the measurement chain reliably captures these high-amplitude events, despite the fact that their exact peak magnitude cannot be fully resolved within the available ADC range.

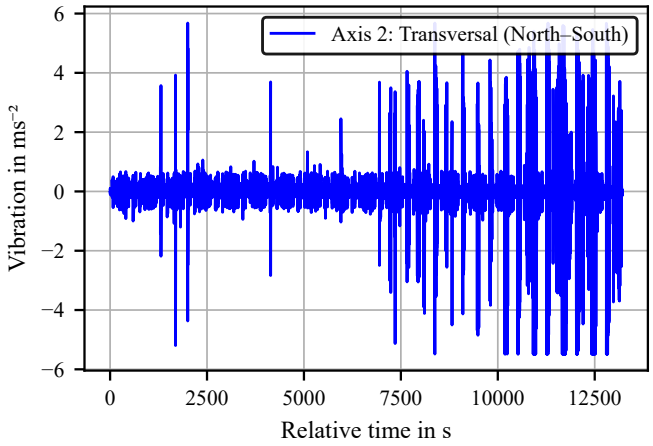

Figure 11. Measured vibration signal of Axis 2 obtained using analogue signal conditioning during the measurement period.

The behaviour characterised by the emergence of pronounced peaks from approximately $t \approx 7{,}500\,\mathrm{s}$ onwards can also be observed in the time–frequency representation shown in Fig. 12. The STFT reveals increasingly strong anomalous events in the frequency domain, particularly from about $t \approx 10{,}000\,\mathrm{s}$ onwards, which appear as distinct vertical high-intensity structures (yellow bands) in the spectrogram. These vertical structures indicate short-duration impulsive events whose energy is distributed across a broad frequency range, which is characteristic of transient mechanical disturbances rather than steady-state vibration components.

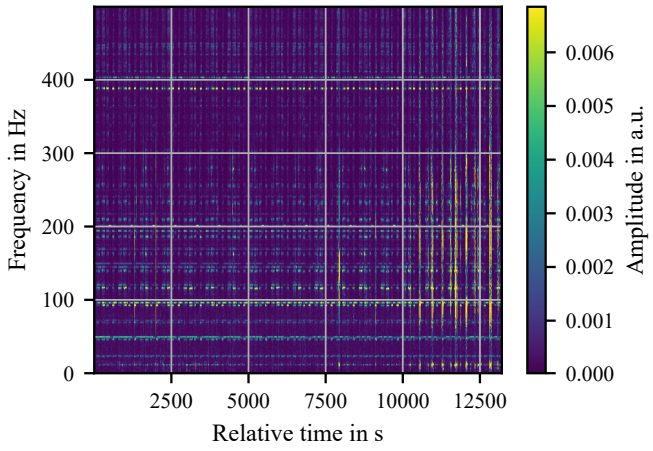

Figure 12. Short-time Fourier transform (STFT) of the vibration signal of Axis 2 (cf. Fig. 11).

For both axes, in addition to the transversal (North–South) vibration components shown in Fig. 10 or Fig. 11 and Fig. 12 respectively, a similar temporal trend in each case is also present in the other two measured vibration directions, albeit with a weaker amplitude. The transversal vibration component is presented here, as it exhibits the anomalies most clearly.

Magnetic Field Strength Analysis In addition to the vibration analysis, the magnetic field of the drive unit of the 12023-heliostat is investigated. This analysis focuses on Axis 2, as the previous vibration analysis has already identified Axis 2 as the primary source of the observed anomalies, with the effects measured on Axis 1 most likely resulting from mechanical coupling between the two axes.

In contrast to the vibration signals, the effects emerging for $t \gtrsim 7{,}500\,\mathrm{s}$ are less pronounced in the magnetic field strength signals. Instead of a global overview of the entire measurement period, as shown for the vibration data in Fig. 10 and Fig. 11, a comparative perspective between the early and late stages of the measurement period is more appropriate. This comparison is shown in Fig. 13, where the magnetic field signal recorded near the start of the measurement at approximately $t \approx 500\,\mathrm{s}$ (blue curve) is compared with the signal recorded near the end of the measurement at $t \approx 12{,}500\,\mathrm{s}$ (orange curve).

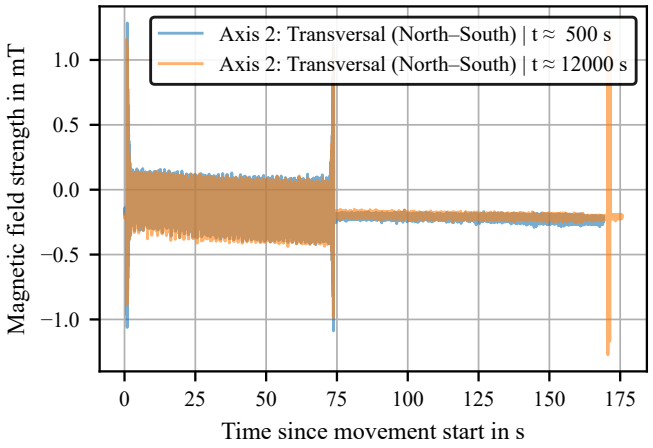

Figure 13. Time-domain comparison of early-stage and late-stage measurements obtained using analogue signal conditioning. It should be noted that the x-axis shows the time since movement start. (I.e. measurements were recorded at different points in time, but both segments are aligned to start at $t = 0\,\mathrm{s}$.).

In the left half of the time series shown in Fig. 13 (i.e. 0–75 s after movement start), in both cases, two pronounced peaks can be observed in the magnetic field signal, corresponding to the motor start-up and braking phases, during which the motor current generates the strongest magnetic field. Between these peaks, the signal exhibits a quasi-stationary phase associated with steady motor operation. In this time-domain representation, both curves appear largely similar.

In the right half of the time series shown in Fig. 13 (i.e. 75–175 s after movement start), it can be observed that an additional motor correction movement occurs at the later measurement time, which is visible as the prominent orange peak. This indicates that when the vibration levels become elevated, as observed previously (cf. Fig. 10 or Fig. 11 and

Fig. 12), the heliostat performs additional automatic correction movements because the target position cannot be reached with sufficient accuracy. Consequently, such peaks in the magnetic field strength signal can also be interpreted as indicators of operational problems of the drive units.

A comparative frequency-domain analysis is performed with the corresponding FFT results shown in Fig. 14. In contrast to the time-domain representation in Fig. 13, clear differences between the blue and the orange curve become visible in the frequency domain in the low-frequency range ($0\,\mathrm{Hz} < f < 80\,\mathrm{Hz}$). In this frequency range, the late-stage measurement (orange curve) exhibits noticeably higher amplitudes and a larger number of discrete spectral peaks compared with the early-stage measurement (blue curve). The same behaviour is observed when analysing additional time segments beyond the representative comparison ($t \approx 500\,\mathrm{s}$ and $t \approx 12{,}500\,\mathrm{s}$) considered so far. In agreement with the vibration results presented earlier, these observations indicate that the spectral changes emerge distinctly for $t \gtrsim 7{,}500\,\mathrm{s}$, suggesting the onset of a pronounced degradation regime rather than a slowly evolving, continuously increasing trend. In contrast, no comparable behaviour is observed for Axis 1. In this case, the spectra of the early-stage and late-stage measurements largely overlap across the analysed frequency range, apart from minor fluctuations attributable to measurement noise. Furthermore, the higher-frequency range up to $500\,\mathrm{Hz}$ (corresponding to the Nyquist limit of the acquisition system) was also examined but did not reveal similarly pronounced differences.

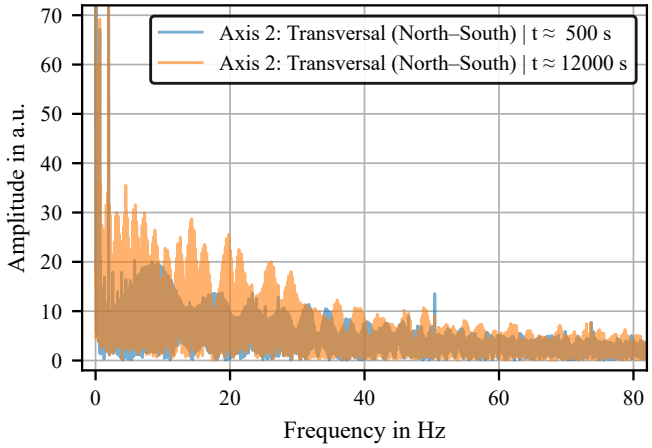

Figure 14. FFT-based comparison of early-stage and late-stage measurements shown in Fig. 13.

Evaluation of Wind Influence on the Measurements It should be noted that wind constitutes a significant external excitation source affecting heliostat behaviour, as discussed in previous studies (Emes et al., 2021; Luo, Li, & Xiong, 2021; Pfahl et al., 2017; Blume, Röger, Schlichting, Macke, & Pitz-Paal, 2020). To ensure that the observed signal patterns in the measurement data originate from operational problems of the drive units rather than from wind-induced structural vibrations, several filtering and verification steps are applied during the analysis.

Firstly, the measurement data recorded during strong-wind conditions is excluded from further evaluation. Secondly, the wind strength during the measurement period is classified, and it is observed that the wind strength was low on this particular measurement day, with peak wind speeds of approximately $10\,\mathrm{m\,s^{-1}}$ ("fresh breeze" according to the Beaufort scale) and predominantly below $8\,\mathrm{m\,s^{-1}}$ ("moderate breeze"). Thirdly, the temporal correlation between wind measurements and the recorded vibration signals is examined, and it is found that there is no correlation at all. Therefore, it can be concluded that the effects and patterns identified in the measurement data presented in this subsection are not wind-induced.

Evaluation of Further External Influences on the Measurements In this paragraph, further external influences are evaluated to assess whether the observed signal patterns in the measurement data potentially could have been caused by factors other than a local drive unit related disturbance. However, no significant change in ambient temperature was observed during the relevant time period. Additionally, there are no reported disturbances of the overall heliostat field on the day of the measurement that could explain the localised response of the 12023 heliostat. Similarly, no supply voltage or grid fluctuations that could have affected the operation of the heliostat field are known to have occurred during the investigated period.

Other external factors that could influence the operation of the overall solar tower plant have also been considered, such as cloud passages and the resulting short-term spatial variation or reduction in the irradiance focused onto the receiver. However, such effects would be expected to affect the overall heliostat field or larger groups and clusters of heliostats rather than producing the observed signal patterns in the measurement data for a single, isolated heliostat.

All in all, these observations and considerations provide substantial support for the interpretation that the effects and patterns identified in the measurement data are not induced by wind or any other external influence, but originate from the heliostat drive units and reflect genuine operational degradation.

Operational Implications for Prognostics-Based Maintenance Although the heliostat remained operational throughout the entire measurement period of $T \approx 13{,}000\,\mathrm{s}$ ($\approx 3.6\,\mathrm{h}$) and continued to execute the commanded movements (actuator extending and retracting), the observed ageing-related anoma-

lies indicate that a complete operational failure may occur in the near future. Within the proposed prognostics framework for heliostat drive units, the degradation indicated by the measurement data could serve as an early warning mechanism. Even a simple monitoring strategy based on the detection of abnormal vibration behaviour using low-level thresholds would likely be sufficient to identify the affected heliostat.

Therefore, as an example, the operational problems identified for Axis 2 of the 12023-heliostat would no longer result in an unexpected failure. Instead, the identified deviations provide an early indication of an emerging problem in the Axis 2 drive unit, enabling O&M personnel to initiate targeted inspection, root-cause analysis and specific maintenance actions.

4.4. Cost Comparison of the Arduino Monitoring Architecture Relative to Heliostat Total Costs

A rough cost comparison between the proposed cost-efficient measurement architecture and a conventional industrial-grade sensor and datalogger setup is performed and. This yields a cost reduction factor of roughly 70 for the instrumentation of a single heliostat. (Arduino-based system incl. 3-axis acceleration sensor, Hall-effect sensor, analogue signal conditioning, Arduino GIGA microcontroller approximately 105 € vs. conventional measurement setup incl. PC oscilloscope, current clamps, industrial-grade vibration measurement system with sensor and data logger approximately 7,400 €). All prices correspond to typical market values in Germany in the second half of 2025. In both cases, an additional measurement computer is required for measurement control and data acquisition.

Although the values presented here have to be regarded as indicative order-of-magnitude estimates rather than a detailed economic analysis, the cost-difference by the factor of 70 remains substantial. This becomes particularly relevant in utility-scale fields with 10^3–10^5 heliostats, making scalability essential.

To put these calculated costs into context, literature studies (Pfahl, Randt, Holze, & Unterschütz, 2013; Blackmon, 2013; Kurup, Akar, Glynn, Augustine, & Davenport, 2022) report estimated or target heliostat costs in the range of approximately 75 USD – 127 USD m^{-2} of reflective area resulting in heliostat costs of roughly 500 € – 880 € per heliostat. (For this brief calculation, an exchange rate of 1 USD $\approx$ 0.86 € and about $8\,\mathrm{m}^2$ per heliostat - as in the heliostat field of the solar tower research facility in Jülich (Göhring et al., 2023) - has been assumed.) Therefore, under these simplified assumptions, the hardware costs of the Arduino-based monitoring system of 105 € correspond to approximately 11–21 % of the total heliostat costs. Although not a full economic assessment, this estimate indicates that sensor costs at this level become a significant factor when monitoring large numbers of heliostats. Future developments may further reduce costs through highly integrated, industrially manufactured sensor modules combining sensing, signal conditioning, and microcontroller functionality on a single board.

Looking toward future developments, solar tower technology nowadays represents a comparatively small but established segment of CST deployment (International Renewable Energy Agency (IRENA), 2024). As of 2023, approximately $1{,}802\,\mathrm{MW}$ of solar tower capacity was installed worldwide across 34 projects, with a median solar field area of about $208{,}240\,\mathrm{m}^2$ per plant (Alami et al., 2023). At the same time, the Chinese market is currently experiencing rapid growth, with approximately $6.72\,\mathrm{GW}$ of solar tower capacity under construction or planned as of 2025 (Lynch, Metghalchi, & Levendis, 2025). In such large-scale deployments, cost- efficient solutions become increasingly essential for scalable monitoring of heliostat drive units in heliostat fields.

5. CONCLUSION AND OUTLOOK

Summary of this Work This study presents the conception, development, and experimental validation of a cost-efficient prognostics framework for heliostat drive units. Existing research on heliostat operation and maintenance has mainly addressed optical performance aspects, wind-induced effects as well as tracking and calibration methods. However, experimental investigations of monitoring concepts for heliostat drive units remain largely absent in the literature. The experimental results obtained during a measurement campaign at the DLR solar tower research facility in Jülich, Germany, demonstrate that the proposed cost-efficient prognostics framework for heliostat drive units enables the identification of emerging degradation during operation. Detecting deviations in the operational data at an early stage of time allows degradation processes to be addressed in a controlled manner before functional failures occur, thereby improving operational safety of the plant and reducing the risk of unplanned outages. All in all, this supports the reliable and economically efficient operation of large heliostat fields as part of critical energy infrastructure. While developed and validated for heliostat drive units, the proposed monitoring methodology may also be transferable to other electromechanical systems in industrial PHM applications.

Further Evaluation Requirements and Current Limitations While this study demonstrates the feasibility of the proposed monitoring approach, further systematic validation is required to assess the robustness and long-term reliability of the prognostics framework under extended field operation and outdoor exposure. Environmental influences, sensor ageing, cable degradation, a potential long-term signal drift as well as practically unavoidable installation-related variations in sensor placement/ orientation and coupling to the drive unit may affect measurement stability and therefore require further investigation. Additional aspects to be addressed in

future studies regarding future deployment of the prognostics framework include automated sensor calibration, robust communication, data integrity, cybersecurity and integration into plant-level O&M infrastructures. Moreover, while the present work shows the detectability of condition-sensitive changes in operational sensor data, it does not yet provide a validated degradation model or a remaining useful life (RUL) prediction for the heliostat drive units.

Ongoing and Future Experimental Work Indicating the significant potential for future investigations, an additional measurement campaign - beyond the results mentioned and discussed in this study - is already being conducted at the solar tower research facility in Jülich. This ongoing measurement campaign extends the present study by investigating both field-wide scalability options for the proposed monitoring concept, as well as the behaviour of heliostat drive units when subjected to controlled artificial ageing and deliberate stress. Generating fault- and degradation-related data on demand reduces the dependence on rare, naturally occurring operational failures, enabling a more systematic analysis of stress–response relationships in heliostat drive units. Moreover, future work may extend the measurement architecture towards wireless communication, battery-powered operation, local data storage, and edge-computing capabilities. These developments could enable real-time signal processing and data reduction directly at the heliostat, could reduce communication bandwidth requirements, and could facilitate scalable distributed monitoring architectures for large heliostat fields.

Contribution of this work for the field of PHM The main contribution of this study to the field of PHM is the extension of condition monitoring and prognostics concepts to heliostat drive units in solar tower plants, a topic that has received limited attention in PHM research so far. By addressing these kinds of large-scale, outdoor-exposed renewable power plants, the present work expands the scope of PHM applications to infrastructure where reliability, scalability, and O&M efficiency are directly linked to resilient low-carbon energy provision for electricity generation, high-temperature industrial process heat, and thermochemical applications. The study proves that cost-effective sensor measurements (for example, using an Arduino) enable the detection of deviations related to health state of heliostat drive units within the corresponding operational data. This lays the groundwork for future PHM models in this domain. The cost-efficient prognostic framework presented provides a robust foundation for transitioning from post-failure or periodic inspections to condition-based, predictive maintenance strategies. This transition improves asset management and ultimately contributes to reducing the levelised cost of electricity (LCOE) of solar power tower plants.

CREDIT AUTHORSHIP CONTRIBUTION STATEMENT

Dominik Steinberg: Conceptualisation, Software, Validation, Formal analysis, Investigation, Data Curation, Visualisation, Writing – Original draft, Writing – Review & Editing, Project Administration.
Stefan Huestegge: Methodology, Software, Validation, Formal analysis, Investigation, Data Curation, Visualisation.
Daniel Maldonado: Supervision, Resources, Funding acquisition.
Marc Röger: Supervision, Funding acquisition.
Benedikt Kölsch: Supervision, Funding acquisition.
Robert Pitz-Paal: Supervision, Funding acquisition.

REFERENCES

Achouch, M., Dimitrova, M., Ziane, K., Sattarpanah Karganroudi, S., Dhouib, R., Ibrahim, H., & Adda, M. (2022). On predictive maintenance in industry 4.0: Overview, models, and challenges. *Applied Sciences*, *12*(16). Retrieved from https://www.mdpi.com/2076-3417/12/16/8081 doi: 10.3390/app12168081

Alami, A. H., Olabi, A., Mdallal, A., Rezk, A., Radwan, A., Rahman, S. M. A., ... Abdelkareem, M. A. (2023). Concentrating solar power (csp) technologies: Status and analysis. *International Journal of Thermofluids*, *18*, 100340. Retrieved from https://www.sciencedirect.com/science/article/pii/S2666202723000599 doi: https://doi.org/10.1016/j.ijft.2023.100340

Ali, A., & Abdelhadi, A. (2022). Condition-based monitoring and maintenance: State of the art review. *Applied Sciences*, *12*(2). Retrieved from https://www.mdpi.com/2076-3417/12/2/688 doi: 10.3390/app12020688

Aoun, A., Ilinca, A., Ghandour, M., & Ibrahim, H. (2021). A review of industry 4.0 characteristics and challenges, with potential improvements using blockchain technology. *Computers & Industrial Engineering*, *162*, 107746. Retrieved from https://www.sciencedirect.com/science/article/pii/S0360835221006501 doi: https://doi.org/10.1016/j.cie.2021.107746

Arduino datasheet. (2026). Arduino GIGA R1 WiFi User Manual [Computer software manual]. Retrieved 2026-06-03, from https://docs.arduino.cc/resources/datasheets/ABX00063-datasheet.pdf

Ashley, T., Carrizosa, E., & Fernández-Cara, E. (2019). Heliostat field cleaning scheduling for solar power tower plants: A heuristic approach. *Applied Energy*, *235*, 653-660. Retrieved from https://www.sciencedirect.com/science/article/pii/S0306261918317100 doi:

https://doi.org/10.1016/j.apenergy.2018.11.004

Bakhshipour, S., Emes, M. J., & Arjomandi, M. (2026). Local pressure distributions on a heliostat facet and its strouhal number in turbulent flow. *Solar Energy*, *307*, 114267. Retrieved from https://www.sciencedirect.com/science/article/pii/S0038092X25010308 doi: https://doi.org/10.1016/j.solener.2025.114267

Binali, R., Demirpolat, H., Kuntoğlu, M., Makhesana, M., Yaghoubi, S., & Sayın Kul, B. (2024). A comprehensive review on low-cost mems accelerometers for vibration measurement: Types, novel designs, performance evaluation, and applications. *Journal of Molecular and Engineering Materials*, *12*(03), 2430002. Retrieved from https://doi.org/10.1142/S225123732430002X doi: 10.1142/S225123732430002X

Blackmon, J. B. (2013). Parametric determination of heliostat minimum cost per unit area. *Solar Energy*, *97*, 342-349. Retrieved from https://www.sciencedirect.com/science/article/pii/S0038092X13003423 doi: https://doi.org/10.1016/j.solener.2013.08.032

Blackmon, J. B. (2014). Heliostat drive unit design considerations – site wind load effects on projected fatigue life and safety factor. *Solar Energy*, *105*, 170-180. Retrieved from https://www.sciencedirect.com/science/article/pii/S0038092X14001339 doi: https://doi.org/10.1016/j.solener.2014.02.045

Blume, K., Röger, M., & Pitz-Paal, R. (2023). Full-scale investigation of heliostat aerodynamics through wind and pressure measurements at a pentagonal heliostat. *Solar Energy*, *251*, 337-349. Retrieved from https://www.sciencedirect.com/science/article/pii/S0038092X22008878 doi: https://doi.org/10.1016/j.solener.2022.12.016

Blume, K., Röger, M., Schlichting, T., Macke, A., & Pitz-Paal, R. (2020). Dynamic photogrammetry applied to a real scale heliostat: Insights into the wind-induced behavior and effects on the optical performance. *Solar Energy*, *212*, 297-308. Retrieved from https://www.sciencedirect.com/science/article/pii/S0038092X20311154 doi: https://doi.org/10.1016/j.solener.2020.10.056

Calabrese, F., Regattieri, A., Bortolini, M., Gamberi, M., & Pilati, F. (2021). Predictive maintenance: A novel framework for a data-driven, semi-supervised, and partially online prognostic health management application in industries. *Applied Sciences*, *11*(8). Retrieved from https://www.mdpi.com/2076-3417/11/8/3380 doi: 10.3390/app11083380

Cannavacciuolo, L., Ferraro, G., Ponsiglione, C., Primario, S., & Quinto, I. (2023). Technological innovation-enabling industry 4.0 paradigm: A systematic literature review. *Technovation*, *124*, 102733. Retrieved from https://www.sciencedirect.com/science/article/pii/S0166497223000445 doi: https://doi.org/10.1016/j.technovation.2023.102733

Emes, M., Jafari, A., Pfahl, A., Coventry, J., & Arjomandi, M. (2021). A review of static and dynamic heliostat wind loads. *Solar Energy*, *225*, 60-82. Retrieved from https://www.sciencedirect.com/science/article/pii/S0038092X21005831 doi: https://doi.org/10.1016/j.solener.2021.07.014

Failing, J. M., Abellán-Nebot, J. V., Benavent Nácher, S., Rosado Castellano, P., & Romero Subirón, F. (2023). A tool condition monitoring system based on low-cost sensors and an iot platform for rapid deployment. *Processes*, *11*(3). Retrieved from https://www.mdpi.com/2227-9717/11/3/668 doi: 10.3390/pr11030668

Göhring, F., Kaufhold, O., Quinto, D. M., Sibum, M., & Wirger, M. (2023). Operational experiences with the heliostat field at the Juelich solar towers. In G. Zhu, M. Röger, & Z. Wang (Eds.), *Advances in solar energy: Heliostat systems design, implementation, and operation* (Vol. 12671, p. 1267109). SPIE. Retrieved from https://doi.org/10.1117/12.2677417 doi: 10.1117/12.2677417

Griffith, D., Moya, A., Ho, C., & Hunter, P. (2011, 01). Structural dynamics testing and analysis for design evaluation and monitoring of heliostats. *Journal of Solar Energy Engineering*, *137*. Retrieved from https://doi.org/10.1115/ES2011-54222 doi: 10.1115/ES2011-54222

Hasibuzzaman, M., Shufian, A., Shefa, R., Raihan, R., Ghosh, J., & Sarker, A. (2020, June). Vibration measurement & analysis using arduino-based accelerometer. In *Ieee region 10 symposium (tensymp)*. IEEE. Retrieved from https://doi.org/10.1109/TENSYMP50017.2020.9230668 doi: 10.1109/TENSYMP50017.2020.9230668

Hossain, M. S., Ali Bashir, M. B., & Akter, K. (2026). Design a low-cost solar pv data logger and assess the application and accuracy with off-grid monocrystalline panels. *Measurement*, *258*, 119176. Retrieved from https://www.sciencedirect.com/science/article/pii/S0263224125025357 doi: https://doi.org/10.1016/j.measurement.2025.119176

Huang, C., Bu, S., Lee, H. H., Chan, C. H., Kong, S. W., & Yung, W. K. (2024). Prognostics and health management for predictive maintenance: A review. *Journal of Manufacturing Systems*, *75*, 78-101. Retrieved from https://www.sciencedirect.com/science/article/pii/S0278612524001183 doi:

https://doi.org/10.1016/j.jmsy.2024.05.021

Ilse, K., Micheli, L., Figgis, B. W., Lange, K., Daßler, D., Hanifi, H., ... Bagdahn, J. (2019). Techno-economic assessment of soiling losses and mitigation strategies for solar power generation. *Joule*, *3*(10), 2303-2321. Retrieved from https://www.sciencedirect.com/science/article/pii/S2542435119304222 doi: https://doi.org/10.1016/j.joule.2019.08.019

International Renewable Energy Agency (IRENA). (2024). *Renewable capacity statistics 2024* (Tech. Rep.). Abu Dhabi: International Renewable Energy Agency. Retrieved from https://www.irena.org/-/media/Files/IRENA/Agency/Publication/2024/Jul/IRENA_Renewable_Energy_Statistics_2024.pdf

Jakobsen, M. O. (2024). Low cost mems accelerometer and microphone based condition monitoring sensor, with lora and bluetooth low energy radio. *HardwareX*, *18*, e00525. Retrieved from https://www.sciencedirect.com/science/article/pii/S2468067224000191 doi: https://doi.org/10.1016/j.ohx.2024.e00525

Jundi, Z. S., Al-Waeli, A. H., & Switzner, N. T. (2026). A systematic review of low-cost photovoltaic monitoring systems: Technologies, challenges, and opportunities. *Renewable and Sustainable Energy Reviews*, *226*, 116417. Retrieved from https://www.sciencedirect.com/science/article/pii/S1364032125010901 doi: https://doi.org/10.1016/j.rser.2025.116417

Kolok, P., Hodoň, M., Ševčík, P., Hotz, L., & Remy, N. (2025). Low-cost iot-based predictive maintenance using vibration. *Sensors*, *25*(21). Retrieved from https://www.mdpi.com/1424-8220/25/21/6610 doi: 10.3390/s25216610

Komarizadehasl, S., Mobaraki, B., Ma, H., Lozano-Galant, J.-A., & Turmo, J. (2021). Development of a low-cost system for the accurate measurement of structural vibrations. *Sensors*, *21*(18). Retrieved from https://www.mdpi.com/1424-8220/21/18/6191 doi: 10.3390/s21186191

Kurup, P., Akar, S., Glynn, S., Augustine, C., & Davenport, P. (2022). *Cost update: Commercial and advanced heliostat collectors* (Tech. Rep. No. NREL/TP-7A40-80482). Golden, CO, USA: National Renewable Energy Laboratory (NREL). Retrieved from https://www.nrel.gov/docs/fy22osti/80482.pdf

Luo, H., Li, Z., & Xiong, Q. (2021). Study on wind-induced fatigue of heliostat based on artificial neural network. *Journal of Wind Engineering and Industrial Aerodynamics*, *217*, 104750. Retrieved from https://www.sciencedirect.com/science/article/pii/S0167610521002294 doi: https://doi.org/10.1016/j.jweia.2021.104750

Lynch, B., Metghalchi, H., & Levendis, Y. (2025, 10). Concentrating solar thermal power in china: 2025 review and outlook. *ASME Open Journal of Engineering*, *4*, 040807. Retrieved from https://doi.org/10.1115/1.4070013 doi: 10.1115/1.4070013

Moreno-Cruz, I., Paredes-Orta, C., Martell-Chávez, F., & Salgado-Tránsito, I. (2025). Heliostat drift prediction model to improve heliostat position control in solar fields. *Solar Energy*, *289*, 113323. Retrieved from https://www.sciencedirect.com/science/article/pii/S0038092X25000866 doi: https://doi.org/10.1016/j.solener.2025.113323

Mykoniatis, K. (2020). A real-time condition monitoring and maintenance management system for low voltage industrial motors using internet-of-things. *Procedia Manufacturing*, *42*, 450-456. Retrieved from https://www.sciencedirect.com/science/article/pii/S2351978920306090 (International Conference on Industry 4.0 and Smart Manufacturing (ISM 2019)) doi: https://doi.org/10.1016/j.promfg.2020.02.050

Nkinyam, C. M., Ujah, C. O., Asadu, C. O., Anyaka, B., & Olubambi, P. A. (2025). Development of a low-cost monitoring device for solar electric (pv) system using internet of things (iot). *Results in Engineering*, *28*, 107324. Retrieved from https://www.sciencedirect.com/science/article/pii/S2590123025033791 doi: https://doi.org/10.1016/j.rineng.2025.107324

Osman, M., & Qureshi, I. (2025). Review of photovoltaic and concentrated solar technologies including their performance, reliability, efficiency and storage. *Results in Engineering*, *25*, 104424. Retrieved from https://www.sciencedirect.com/science/article/pii/S2590123025005031 doi: https://doi.org/10.1016/j.rineng.2025.104424

Pargmann, M., Maldonado Quinto, D., Schwarzbözl, P., & Pitz-Paal, R. (2021). High accuracy data-driven heliostat calibration and state prediction with pretrained deep neural networks. *Solar Energy*, *218*, 48-56. Retrieved from https://www.sciencedirect.com/science/article/pii/S0038092X21000621 doi: https://doi.org/10.1016/j.solener.2021.01.046

Pfahl, A., Coventry, J., Röger, M., Wolfertstetter, F., Vásquez-Arango, J. F., Gross, F., ... Liedke, P. (2017). Progress in heliostat development. *Solar Energy*, *152*, 3-37. Retrieved from https://www.sciencedirect.com/science/article/pii/S0038092X17301895 (Progress in Solar Energy Special Issue: Concentrating Solar Power (CSP)) doi: https://doi.org/10.1016/j.solener.2017.03.029

Pfahl, A., Randt, M., Holze, C., & Unterschütz, S. (2013). Autonomous light-weight heliostat with rim drives. *Solar Energy*, *92*, 230-240. Retrieved from https://www.sciencedirect.com/science/article/pii/S0038092X13001023 doi: https://doi.org/10.1016/j.solener.2013.03.005

Sarver, T., Al-Qaraghuli, A., & Kazmerski, L. L. (2013). A comprehensive review of the impact of dust on the use of solar energy: History, investigations, results, literature, and mitigation approaches. *Renewable and Sustainable Energy Reviews*, *22*, 698-733. Retrieved from https://www.sciencedirect.com/science/article/pii/S136403211300021X doi: https://doi.org/10.1016/j.rser.2012.12.065

Sattler, J. C., Röger, M., Schwarzbözl, P., Buck, R., Macke, A., Raeder, C., & Göttsche, J. (2020). Review of heliostat calibration and tracking control methods. *Solar Energy*, *207*, 110-132. Retrieved from https://www.sciencedirect.com/science/article/pii/S0038092X20306447 doi: https://doi.org/10.1016/j.solener.2020.06.030

Schnerring, A., Broda, R., Nieslony, M., Algner, N., Saez Martinez, E., Röger, M., ... Pitz-Paal, R. (2026). Airborne real-time solar concentrator orientation estimation for heliostat coarse calibration. *Solar Energy*, *310*, 114495. Retrieved from https://www.sciencedirect.com/science/article/pii/S0038092X26001830 doi: https://doi.org/10.1016/j.solener.2026.114495

Schnerring, A., Broda, R., Winter, A., Nieslony, M., Krauth, J. J., Röger, M., ... Pitz-Paal, R. (2025). A simulation environment for uav-based real-time condition monitoring of solar tower power plants. *Solar Energy*, *300*, 113803. Retrieved from https://www.sciencedirect.com/science/article/pii/S0038092X25005663 doi: https://doi.org/10.1016/j.solener.2025.113803

Soto-Ocampo, C. R., Mera, J. M., Cano-Moreno, J. D., & Garcia-Bernardo, J. L. (2020). Low-cost, high-frequency, data acquisition system for condition monitoring of rotating machinery through vibration analysis-case study. *Sensors*, *20*(12). Retrieved from https://www.mdpi.com/1424-8220/20/12/3493 doi: 10.3390/s20123493

Stengler, J., Bülow, M., & Pitz-Paal, R. (2025). Concentrating solar technologies for low-carbon energy. *Nature Reviews Clean Technology*, *1*(10), 719–733. Retrieved from https://doi.org/10.1038/s44359-025-00096-4 doi: 10.1038/s44359-025-00096-4

STM32H747 datasheet. (2026). STM32H747xI/G Datasheet [Computer software manual]. Retrieved 2026-06-03, from https://www.st.com/resource/en/datasheet/stm32h747ai.pdf

Tian, M., Chidambaranathan, K., Rafique, M. Z. E., Desai, N., Bai, J., Brost, R., ... Yao, Y. (2026). Heliostat optical error inspection with polarimetric imaging drone. *Solar Energy*, *304*, 114185. Retrieved from https://www.sciencedirect.com/science/article/pii/S0038092X2500948X doi: https://doi.org/10.1016/j.solener.2025.114185

Tiboni, M., Remino, C., Bussola, R., & Amici, C. (2022). A review on vibration-based condition monitoring of rotating machinery. *Applied Sciences*, *12*(3). Retrieved from https://www.mdpi.com/2076-3417/12/3/972 doi: 10.3390/app12030972

Villacorta, J. J., del Val, L., Martínez, R. D., Balmori, J.-A., Magdaleno, Á., López, G., ... Basterra, L.-A. (2021). Design and validation of a scalable, reconfigurable and low-cost structural health monitoring system. *Sensors*, *21*(2), 648. Retrieved from https://www.mdpi.com/1424-8220/21/2/648 doi: 10.3390/s21020648

Villarroel, A., Zurita, G., & Velarde, R. (2019). Development of a low-cost vibration measurement system for industrial applications. *Machines*, *7*(1). Retrieved from https://www.mdpi.com/2075-1702/7/1/12 doi: 10.3390/machines7010012

Wette, J., Sutter, F., Enrique-Orts, R., Pérez-García, M., Sánchez-Moreno, R., & Fernández-García, A. (2025). Soiling of solar-field heliostats during operation in concentrating solar thermal plants. *Results in Engineering*, *28*, 107890. Retrieved from https://www.sciencedirect.com/science/article/pii/S2590123025039416 doi: https://doi.org/10.1016/j.rineng.2025.107890

Wolfertstetter, F., Fonk, R., Prahl, C., Röger, M., Wilbert, S., & Fernández-Reche, J. (2020, 12). Airborne soiling measurements of entire solar fields with qfly. *AIP Conference Proceedings*, *2303*(1), 100008. Retrieved from https://doi.org/10.1063/5.0028968 doi: 10.1063/5.0028968

Zio, E. (2022). Prognostics and health management (phm): Where are we and where do we (need to) go in theory and practice. *Reliability Engineering & System Safety*, *218*, 108119. Retrieved from https://www.sciencedirect.com/science/article/pii/S0951832021006153 doi: https://doi.org/10.1016/j.ress.2021.108119